

Isolating and Tracking Noise Sources across an Active Longwall Mine Using Seismic Interferometry

Santiago Rabade^{*1}, Sin-Mei Wu^{1,2}, Fan-Chi Lin¹, and Derrick J. A. Chambers³

ABSTRACT

The ability to monitor seismicity and structural integrity of a mine using seismic noise can have great implication for detecting and managing ground-control hazards. The noise wavefield, however, is complicated by induced seismicity and heavy machinery associated with mining operations. In this study, we investigate the nature of time-dependent noise cross-correlations functions (CCFs) across an active underground longwall coal mine. We analyze one month of continuous data recorded by a surface 17 geophone array with an average station spacing of ~ 200 m. To extract coherent seismic signals, we calculate CCFs between all stations for each 5-min window. Close inspection of all 5-min CCFs reveals waveforms that can be categorically separated into two groups, one with strong and coherent 1–5 Hz signals and one without. Using a reference station pair, we statistically isolate time windows within each group based on the correlation coefficient between each 5-min CCF and the monthly stacked CCF. The daily stacked CCFs associated with a high correlation coefficient show a clear temporal variation that is consistent with the progression of mining activity. In contrast, the daily stacked CCFs associated with a low correlation coefficient remain stationary throughout the recording period in line with the expected persistent background noise. To further understand the nature of the high correlation coefficient CCFs, we perform 2D and 3D back projection to determine and track the dominant noise source location. Excellent agreement is observed on both short (5-min) and long (daily) time scales between the CCF determined source locations, the overall migration of the active mining operation, and cataloged seismic event locations. The workflow presented in this study demonstrates an effective way to identify and track mining induced signals, in which CCFs associated with background noise can be isolated and used for further temporal structural integrity investigation.

KEY POINTS

- Isolating the mining activity from background noise is important for passive seismic monitoring.
- We show that seismic interferometry can be used to identify and track mining activity in a longwall mine.
- Our proposed framework can lead to simultaneous monitoring of subsurface seismicity and structure changes.

Supplemental Material

INTRODUCTION

A better understanding of the temporal seismicity migration and structural change in a mining setting is important for hazard mitigation. Traditional seismic passive monitoring focuses on determining the seismic event distribution and source characteristics using observed energetic seismic phases (Eaton, 2018). In the case of underground mines, such a method meets a variety of

objectives, including documenting seismicity, ground motion monitoring, back analysis of significant failures, assessing mine design performance, monitoring kinematics of geological structures, and rockburst hazard management (Mendecki *et al.*, 2010; Swanson *et al.*, 2016; Nordström *et al.*, 2020). A similar approach has also been widely applied in other industrial applications, including hydraulic fracturing (Maxwell *et al.*, 2012), CO₂ and water injection (Verdon *et al.*, 2010), enhanced

1. Department of Geology and Geophysics, University of Utah, Salt Lake City, Utah, U.S.A., <https://orcid.org/0000-0003-1750-489X> (SR); <https://orcid.org/0000-0001-8330-471X> (S-MW); <https://orcid.org/0000-0003-0394-6830> (F-CL); 2. Swiss Seismological Service, ETH Zürich, Zurich, Switzerland; 3. National Institute for Occupational Safety and Health, Spokane, Washington, D.C., U.S.A., <https://orcid.org/0000-0003-3656-6607> (DJAC)

*Corresponding author: san.rabade@utah.edu

Cite this article as Rabade, S., S.-M. Wu, F.-C. Lin, and D. J. A. Chambers (2022). Isolating and Tracking Noise Sources across an Active Longwall Mine Using Seismic Interferometry, *Bull. Seismol. Soc. Am.* **XX**, 1–12, doi: [10.1785/0120220031](https://doi.org/10.1785/0120220031)

© Seismological Society of America

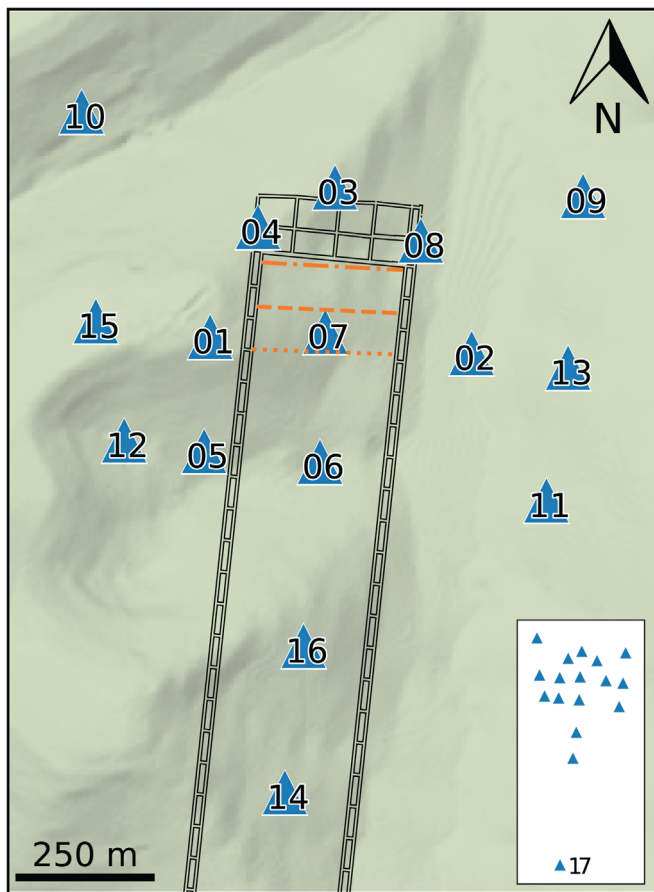


Figure 1. Station location (triangles), and longwall location for days 7/09, 7/16, and 7/26 marked as dash-dotted, dashed, and dotted line, respectively. The solid lines depict the mine structure. The inset shows the full array configuration including one further station. The color version of this figure is available only in the electronic edition.

geothermal systems (Majer *et al.*, 2007), tunnel development (Chen *et al.*, 2011), and several others. Such an approach, however, has some drawbacks. First, it depends on the presence of seismicity, meaning less-active mines (or mining areas) receive no benefit from monitoring and aseismic processes are undetectable. Second, industrial noise associated with mining can severely limit the monitoring system's sensitivity. Third, although automated processing of seismicity is improving, often significant time is required by human analysts to produce high-quality event catalogs.

Seismic interferometry, on the other hand, offers an alternative way to identify changes in seismic source characteristics and structural properties by detecting weaker but coherent seismic signals. A handful of recent works in a mining setting have demonstrated the potential applications of seismic interferometry in underground mine settings. Dales *et al.* (2017a,b) showed seismic interferometry can be used to locate impulsive and persistent sources within mines. They performed synthetic tests and located individual events using seismic waveforms recorded within the mine, obtaining high temporal resolution

using impulsive sources. Czarny *et al.* (2016) used two surface broadband stations several kilometers apart to detect subtle velocity decreases associated with longwall mining and induced seismicity. Lu and Feng (2017) used the conveyor belt as a source to image changes in the mining face.

Outside of mining, studies have also demonstrated noise cross-correlation functions (CCF), in addition to studying the velocity structure by extracting the empirical Green's function (Lobkis and Weaver, 2001; Shapiro *et al.*, 2005; Lin *et al.*, 2008; Nicolson *et al.*, 2014; Spica *et al.*, 2016), can be used to understand the seismic source when transient or persistent noise sources are present (Haney, 2010, 2014; Cros *et al.*, 2011; Ballmer *et al.*, 2013; Wu *et al.*, 2017, 2019, 2021). These applications focus on the extraction of coherent wavefields emitted by the spurious seismic source, which can be used to study the source property (e.g., location) based on the associated time arrivals, amplitudes, and polarizations in the CCFs. Early continental-scale studies have located persistent sources of longer-period surface waves, including the 26 s microseism energy from Gulf of Guinea (Shapiro *et al.*, 2006) and the Kyushu microseism (Zheng *et al.*, 2011). It has also been used to study and find more localized hydrothermal and volcanic tremor activities in Yellowstone (Cros *et al.*, 2011; Wu *et al.*, 2019, 2021), Alaska (Haney, 2010, 2014), Hawaii (Ballmer *et al.*, 2013), and Iceland (Li *et al.*, 2017). Moreover, by exploring the stability of the noise correlation coda signals, temporal structural variation can be also inferred (Brennguier *et al.*, 2008; Clements and Denolle, 2018; Wu *et al.*, 2020). Using seismic interferometry to study temporal source and structure variation in a mine setting nevertheless has not been fully explored.

In this study, we investigate the possibility of using temporal variation of CCFs to resolve changes in source location and velocity structure across an active longwall coal mine. Longwall mining is a method of underground mining that allows the extraction of full slices or panels of mineral resources (Fig. 1). The mining machines consist of one or more shearers or ploughs (cutting instruments) mounted on a series of self-advancing hydraulic ceiling supports. The most common mechanism of the seismicity is a normal fault with a near-vertical plane parallel to the mining wall (Stec, 2007; Bischoff *et al.*, 2010; Sen *et al.*, 2013; Verdon *et al.*, 2018). In addition, the longwall coal seismicity also includes events with non-double-couple sources related to roof caving and events with orientations associated with tectonic features or preexisting faults.

By analyzing data from a 17-station seismic geophone array (Fig. 1) above an active longwall coal mine, we first exploit the use of seismic interferometry to characterize and isolate time windows with different noise properties (i.e., dominated by background noise versus mining induced seismicity). We then migrate the CCF waveforms that contain mining-related seismic energy to obtain the 2D/3D source location using consecutive 24 hr and 5-min time windows throughout the deployment time periods. For both time scales, our results

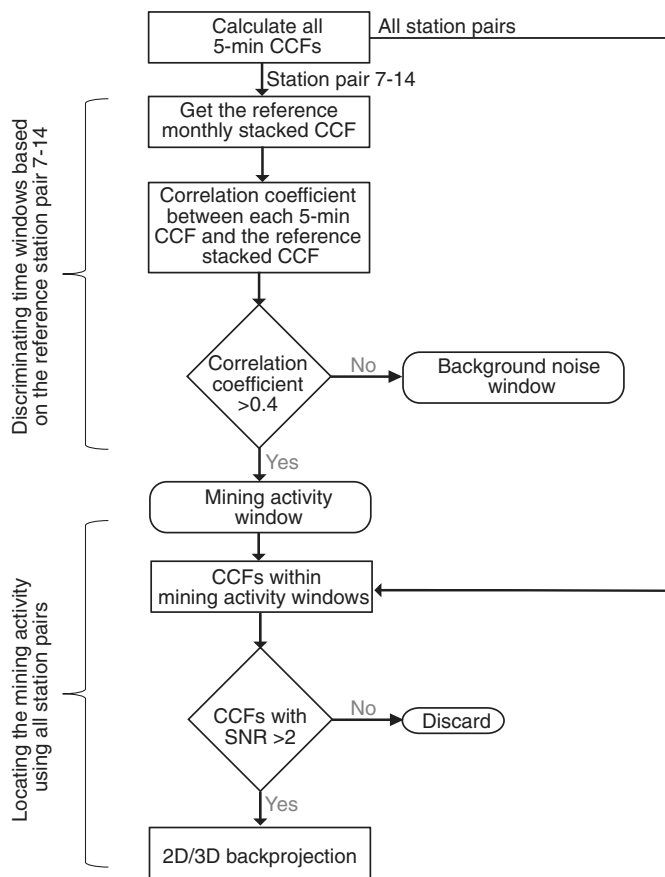


Figure 2. The workflow for the analyses applied in this study.

agree with the position of the overall mining longwall and the cataloged seismicity location. We demonstrate that this workflow (Fig. 2) can be used to monitor seismic activity in complex settings with continuous data recorded on the surface and show how periods of mining-dominated noise can be distinguished from quieter times, which may be useful for structural imaging and monitoring.

DATA

We deployed 17 three-component (3C) autonomous 5 Hz nodal geophones on the surface above and around a longwall coal mine from 30 June to 2 August 2018 (dataset B of Johnson *et al.*, 2021). Of the 17 stations, 14 were deployed close by forming a 1 km by 0.5 km semigridd on top of the active mining area (Fig. 1). The longwall orientation is nearly to east–west, and the approximate length of the mining wall is 250 m. The coal extraction activity moves along from north to south, and during our deployment, it advanced around 200 m south. The mine operator provided the longwall locations as measured by the surveyors every few days. A catalog of approximately 22,000 seismic events is also available (Johnson *et al.*, 2021), with local magnitudes ranging from -1.7 to 1.4 .

The spectrogram of the vertical component at station 7 (Fig. 3) reveals the active nature of the mining environment.

While we see stable and continuous background noise at the secondary microseism band (~ 5 – 10 s; Stehly *et al.*, 2006), we observe sporadic mining-related seismic energy in frequencies higher than 1 Hz. Although these energetic signals likely are associated with the mining induced seismic events, they can also be related to the shearing machinery, ore crushers, or heavy trucks. In the first seven days of July, this high-frequency energy is not as apparent or nearly absent. The activities pick up considerably after 7 July after the long weekend holiday of the United States Independence Day.

METHODS

Cross correlations

To investigate temporal CCF variation, we follow the methodology described by Wu *et al.* (2019, 2021) to first calculate the vertical component 5-min CCFs between all station pairs. Here, we cut the continuous data into 5-min nonoverlapping windows and perform spectral normalization before calculating the CCFs. We then stack the 5-min 1–5 Hz band-passed CCFs into the desired length in time (i.e., hourly stack and daily stack). We focus on the 1–5 Hz frequency band in this study, which presents the most coherent and persistent signals. To retain the relative CCF amplitude across the entire array (Lin *et al.*, 2012; Bowden *et al.*, 2015), each 5-min CCF was normalized based on the 90th percentile maximum amplitude of the CCFs across the entire array for that 5-min window before stacking. We note that although the normalization process is applied to down-weight sporadic but energetic events, persistent events that excited coherent cross-correlation signals can still dominate the stacked CCF.

Figure 4 shows the 5-min CCF variations for station pairs 6–3 and 7–14 on 26 July. Clear and coherent arrivals above the noise level throughout the day can be observed. Most energetic signals arrive close to zero lag time, reflecting the nature of the close station spacing and the fact that some noises originated from mining activities within the array. Close inspection reveals apparent temporal CCF variations particularly when comparing the CCF waveforms from earlier and later during the day (Fig. 4). The 5-min CCFs exhibit a lower signal-to-noise ratio (SNR) during the second half of the day, consistent with the weaker and presumably less coherent 1–5 Hz energy observed in the spectrogram (Fig. 3).

Separating the mining-related energy and the background noise

In addition to SNR, we observed that the CCF waveforms are different between the quiescent and operating time periods (e.g., white traces in Fig. 4a,b). The remarkable difference can be identified based on visual observation and from a single station pair. We also observe that the daily stack (Fig. 4c,d) of all the 5-min windows shows features more related to the mining time than the quiet time suggesting cross-correlation signals excited by mining activities are rather coherent. This

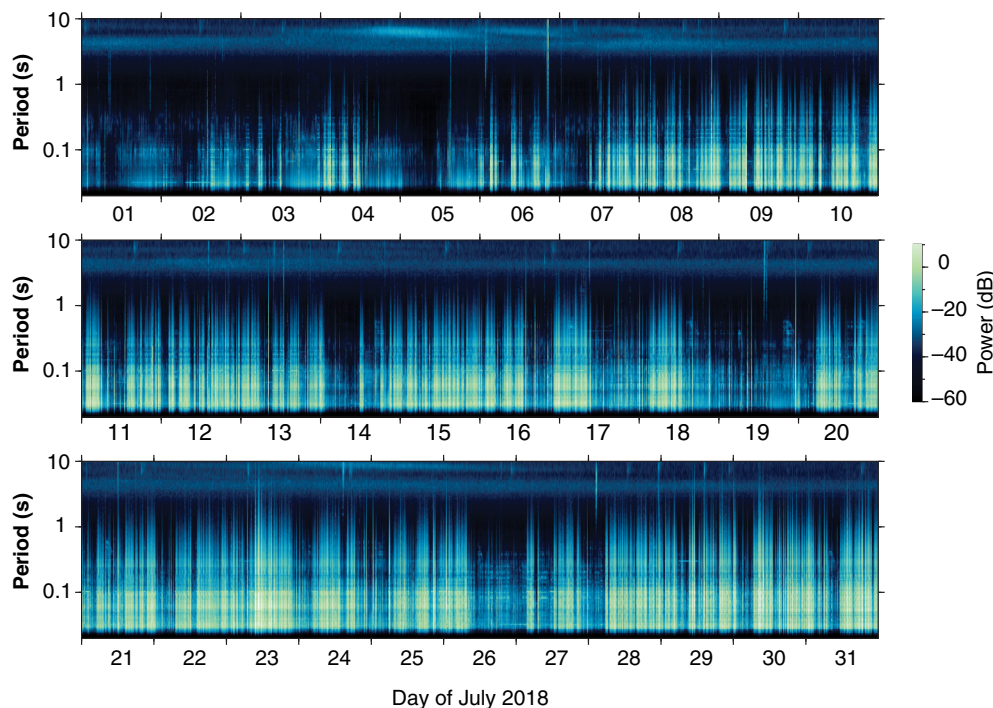


Figure 3. Month-long spectrogram of the vertical component recorded by station 7 (shown in Fig. 1). Power in decibel (dB) units of $10\log_{10}(\text{m}^2/\text{s}^4/\text{Hz})$. The color version of this figure is available only in the electronic edition.

motivates us to isolate the mine activity from the background noise based on the waveform similarity.

We use the correlation coefficient between the monthly stacked CCF and each 5-min CCF of a reference station pair 7–14 to separate the time windows dominated by mine energy (Fig. 5). We choose station pair 7–14 for two reasons. First, station 7 is the closest station to the mining operation and station 14 is outside the active mining area but on the coal extraction axis. Using this station pair, we ensure the 5-min CCFs capture the mining-related energy if present and that the waveform will be consistent during the deployment (Fig. 6b). Second, the interstation distance between the two stations (~ 0.9 km) is large such that there is more complexity in the reference stacked waveform due to slightly offset seismic phases. Assuming seismic signals excited by mining activity are self-similar and dominate the reference stacked CCF, 5-min time windows influenced by mine activity should yield CCFs with higher correlation coefficient. On the other hand, lower correlation coefficients are expected for time windows associated with weaker and less coherent background noise.

Figure 5a summarizes the evolution of the correlation coefficient between 5-min CCFs and the reference CCF for station pair 7–14 over the entire month of July. Low and high correlation coefficients are observed in early and late July, respectively, consistent with the progressive mine extraction operation and recorded seismicity (Fig. 3). A dip in correlation coefficient is observed around 19 July coinciding with the lower seismicity

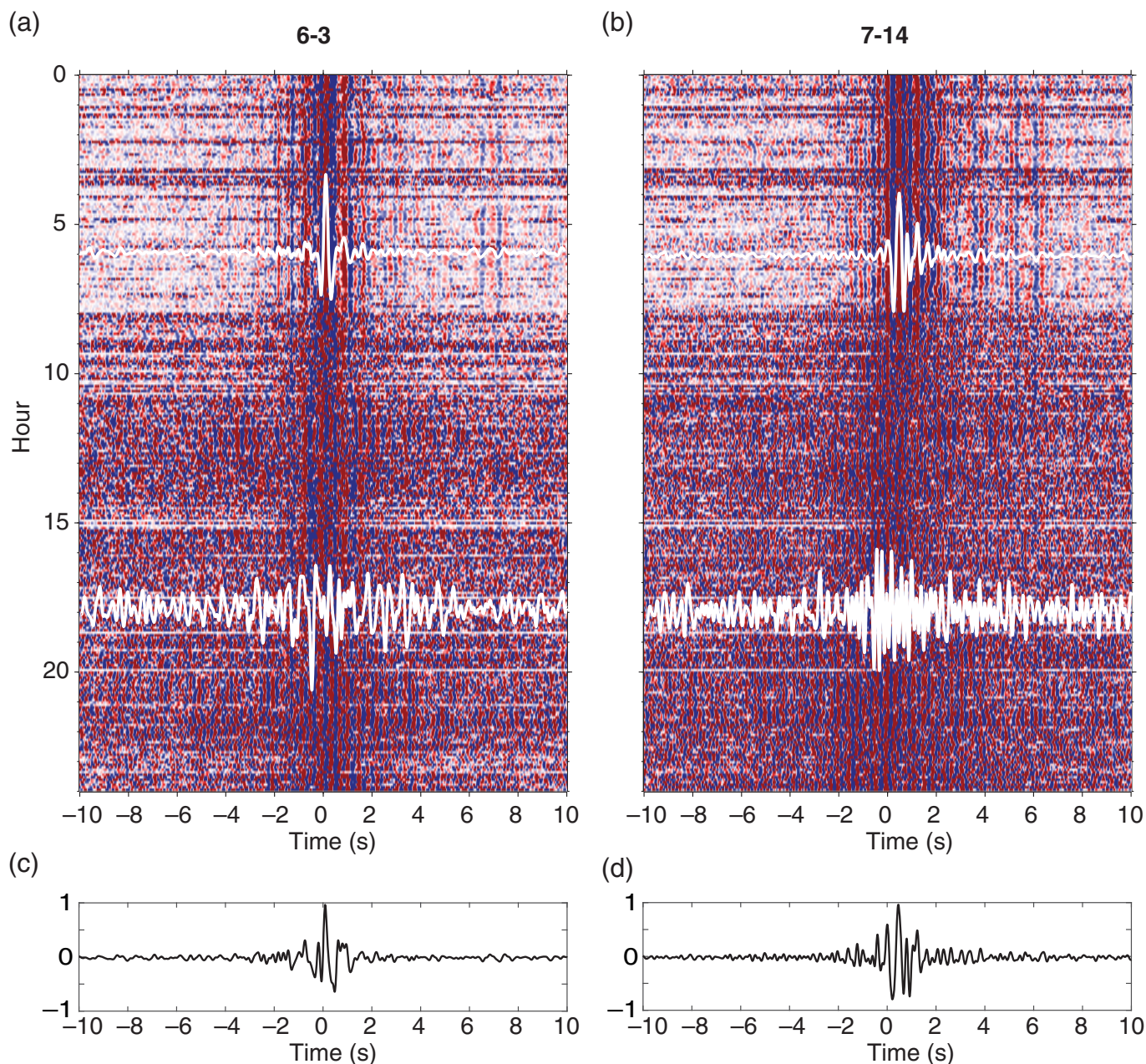
observed around the same time (Fig. 3). This demonstrates the CCF correlation coefficient as an effective indicator for mining induced signals. A simple statistical analysis of the plotted histograms reveals a bimodal distribution of the correlation coefficients from all the 5-min time windows (Fig. 5b). Here we select correlation coefficient of 0.4 to empirically separate all the time windows into two groups.

For each station pair, we stack the CCFs into daily CCFs using the high (>0.4) and low (<0.4) correlation coefficient time windows determined based on the reference station pair 7–14. For station pair 7–14, the daily stack of low correlation coefficient time windows (Fig. 5a) overall shows signals with low SNR. In contrast, the high correlation coefficient

daily stack (Fig. 6b) shows a prominent and steady arrival close to 1 s. The result of station pair 6–3 is shown in Figure 6c,d, where the low correlation coefficient stack shows a stationary waveform between 0 and 1 s lag time throughout the entire period (Fig. 6c). This group of stacked waveforms is consistent with a steady background noise energy during the deployment. In contrast, the high correlation coefficient stack shows a progressive change in the waveform, with the dominant CCF signal shifting from negative time lag at the beginning of July to positive time lag at the end of the same month (Fig. 6d). Here a positive time lag represents seismic sources are closer to the CCF source station (station 6), whereas a negative time lag represents sources are closer to the receiver station (station 3). The change in arrival time for this group of waveforms is in agreement with the progressive movement of the longwall from the north (closer to receiver station 3) to the south (closer to source station 6). The observed stationary and progressively changing waveforms (Fig. 6) suggest that our classification based on correlation coefficient is successful in isolating time windows dominated by mining related signals and background noise.

Locating the mining activity

To further investigate the nature of temporal variations of CCF signal associated with the mining activities, we applied a CCF back projection method to determine the source location (Shapiro *et al.*, 2006; Zheng *et al.*, 2011; Ballmer *et al.*, 2013; Li *et al.*, 2020). For a given reference velocity, the method back



projects seismic energy observed in the CCFs of all station pairs and determines the most likely area of the sources. The method has the advantage of mapping concurrent seismic sources simultaneously and the determined likelihood function would intrinsically account for the imperfect knowledge of the local velocity model and the source mechanism or area (Kao and Shan, 2004). For a single station pair, the migrated amplitudes form a hyperbola-shaped area that illuminates the potential source locations (Zheng *et al.*, 2011).

To determine the appropriate reference velocity for the area, for each 100 m distance bin, we stack all CCFs from a quiet day (7/5) across the entire array with station pair distance within the bin. This stacking process effectively homogenizes the noise source distribution and allows a clear CCF moveout to be observed (Fig. 7). Based on the observed moveout, we take

Figure 4. (a) Temporal variation of 5-min cross-correlations functions (CCFs) of station pair 6–3 on 7/26. Positive and negative CCF amplitudes are shaded in different tones to highlight the coherency through time. The white waveforms are the 5-min CCFs at 6:00 and 18:00. (b) Same as panel (a) but for station pair 7–14, (c) 7/26 daily CCF stack of station pair 6–3, and (d) 7/26 daily CCF stack of station pair 7–14. The color version of this figure is available only in the electronic edition.

1 km/s as the reference velocity for our back projection analysis. Considering that the objective of this work is to obtain the overall temporal and spatial patterns of the seismic energy generated by the mining processes, we do not intend to resolve earth structure based on the observed moveout nor identify the wave type.

To perform 2D back projection, we build a potential source grid centered on station 7 with 0.001° (~ 100 m)

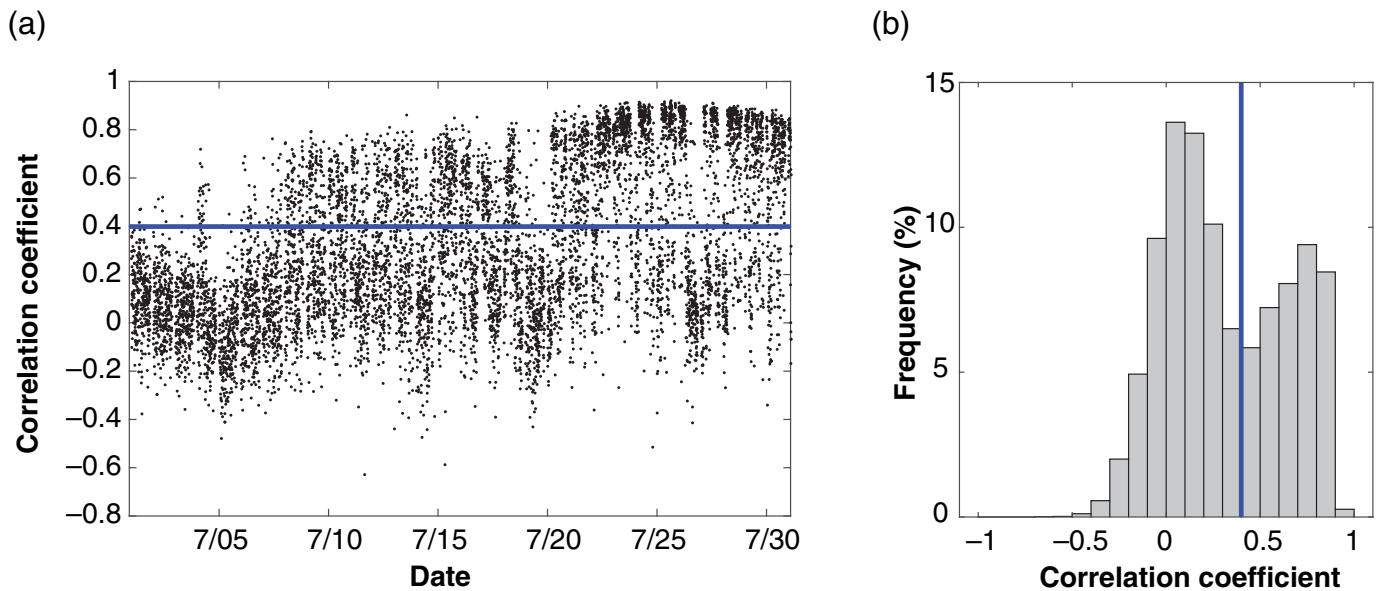


Figure 5. (a) Correlation coefficient between the 5-min CCFs and the monthly stacked CCF for station pair 7–14. The solid line denotes the 0.4 correlation coefficient which roughly separates time windows dominated by mine activity and background noise. (b) Histogram of correlation coefficient from panel (a). The solid line denotes the 0.4 correlation coefficient. The color version of this figure is available only in the electronic edition.

spacing in the north–south and east–west direction. For each potential source grid point, we calculate the expected arrival time for each station based on the straight ray distance. The differential time between any two stations is then used to estimate the expected lag time of the CCF signal for the station pair. For a given station pair, for each grid point, the corresponding amplitude at the expected lag time of the observed CCF normalized envelope function is assigned to the grid point as the likelihood value. By iterating these steps across the entire grid, the process effectively migrates or back-projects the envelope function to a 2D likelihood map (Fig. 8).

The use of the envelope function (instead of the raw CCF waveform) allows us to focus on the migration of seismic energy, which in general produces a more stable and smooth result considering the uncertainties associated with the reference velocity model and source mechanism (Dales *et al.*, 2017a). To further constrain the source locations, we sum all the resulting migrated 2D likelihood maps using all the station pairs with CCF SNR above 2. Here the signal and noise level are defined by the root mean square CCF amplitude within and outside the signal window, respectively. The signal window is determined by the expected minimum and maximum lag time calculated based on the distance and the reference velocity (Fig. 8). After the summation, we normalize the likelihood 2D map based on the maximum value, where areas with higher amplitude indicate the likely source locations (Figs. 9 and 10). Some smoothing is expected due to the finite width of the envelope function and some smearing is also expected for locations close to the edges of the array due to imperfect station coverage.

RESULTS AND DISCUSSION

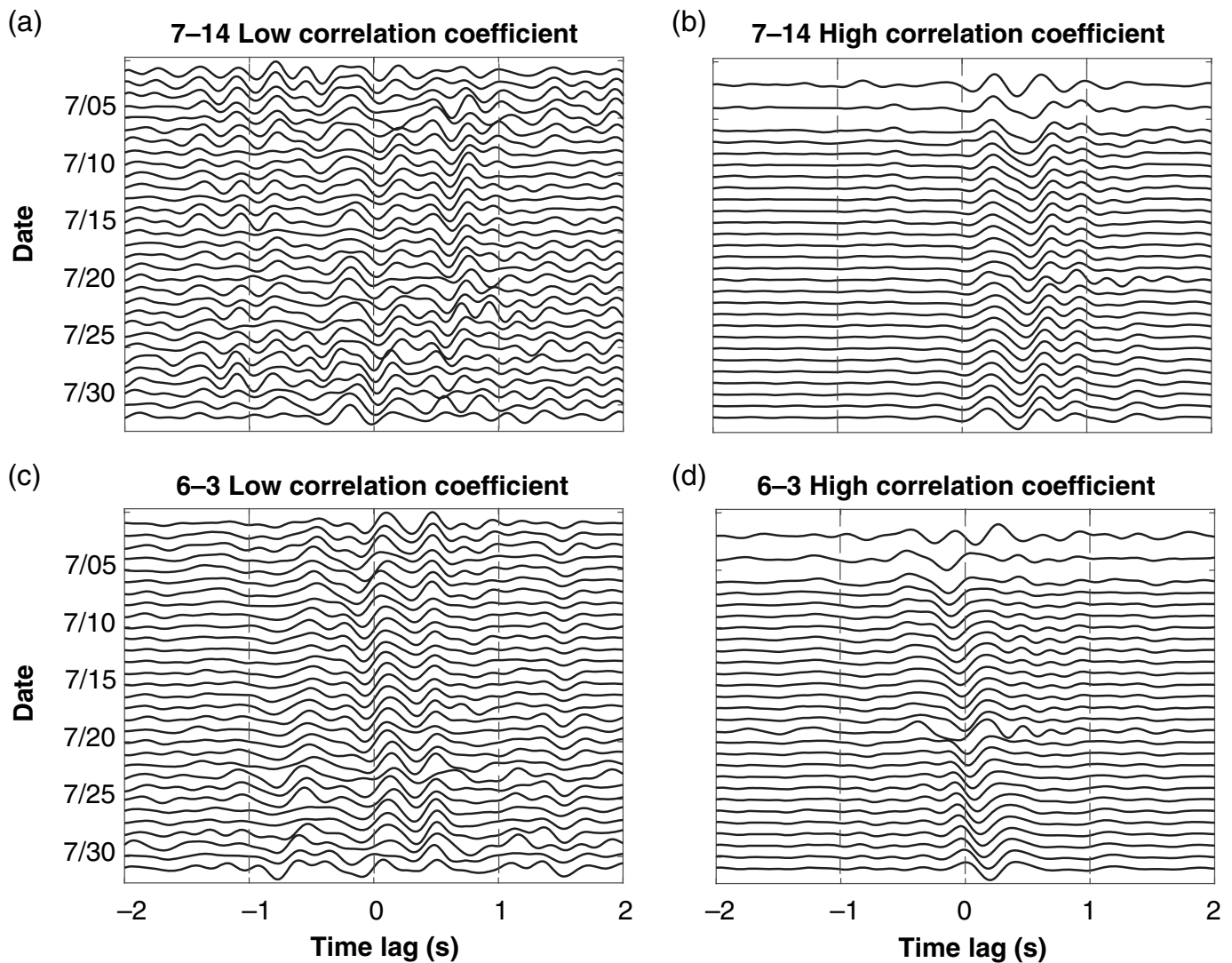
Location from daily and 5-min cross correlations

The 2D back projection images based on the 1–5 Hz daily-stack CCFs reveal a spatial pattern that strongly agrees with the cataloged daily seismicity, a good proxy for the mining

activity, with most of the seismicity contained within the 0.8 contour of the normalized back projection amplitude (Fig. 9 and Movie S1, available in the supplemental material to this article; Johnson *et al.*, 2021). The locations of both the seismicity and the resolved source distribution shift from north to south throughout the deployment period, consistent with the progression of the longwall (Fig. 1).

Compared to the daily stacked waveforms, back projection using 5-min time windows presents the opportunity to track seismicity migration with higher spatiotemporal resolution despite the lower SNR. In Figure 10, results from four example 5-min time windows on 7/26 are presented. Like the daily result, a good correlation between the back projection and the cataloged seismicity is observed. For the case where the seismicity is abundant and clustered (Fig. 10a,b), the area with normalized amplitude larger than 0.9 covers nearly all the event locations. For the rest of the events, the locations are within 0.7 and 0.8 normalized amplitude. For the case with sparser and distributed seismicity (Fig. 10c,d), all the seismicity is located within the area of greater than 0.8 normalized amplitude.

The good agreement between the cataloged seismicity and both the 5-min and daily backprojection results suggests that the interferometry based back projection method performs well, can robustly retrieve the location of the dominant seismic energy, and has the flexibility to tune the time resolution to fulfill different monitoring purposes. Our result in particular implies the framework is suitable for tracking the seismic source



evolution within an active mining environment. Different from the event catalog, which relies on the ability to pick seismic phases for individual events, the interferometry based back projection method presented in this study determines the overall source location during each specific time window. Although the spatiotemporal resolution might not be as high as the event catalog, the interferometry method has the ability to pick up weak but persistent energy and can easily be automated. Rather than a substitute, this method could be used as a complementary tool to better track nonimpulsive energies during mining operation (e.g., longwall operation).

Depth location

In the section [Location From Daily and 5-min Cross Correlations](#), we demonstrate the overall agreement between the cataloged seismicity and our 2D back projection result on both 5-min and daily time scales. Here we explore further whether the method is capable of resolving the source location in 3D. Instead of assuming a 2D wave propagation, we consider body waves as the dominant seismic energy observed in the CCFs

Figure 6. Daily stack for station pair (a,b) 7–14 and (c,d) 6–3. (a,c) Cross correlation with correlation coefficient lower than 0.4. (b,d) Cross correlation with correlation coefficient higher than 0.4.

where straight ray paths again are assumed. We note that as most seismic sources are rather shallow and are directly beneath the seismic array, different wave types (*P* wave, *S* wave, and surface waves) are likely entangled and indistinguishable in the CCFs.

To extend our method to 3D, we add the vertical dimension to the original 2D potential source grid. For each 3D grid point and station, we calculate the source receiver travel time based on the 3D distance and the 1 km/s reference velocity. Here we take the station elevation into account. This change in computation will transform the shape of an individual CCF migration from a 2D hyperbola into a 3D hyperboloid (Fig. 11). Then we apply the same summation process described in the [Locating the mining activity](#) section. Here the amplitude normalization is based on the maximum value of the migrated 3D grid.

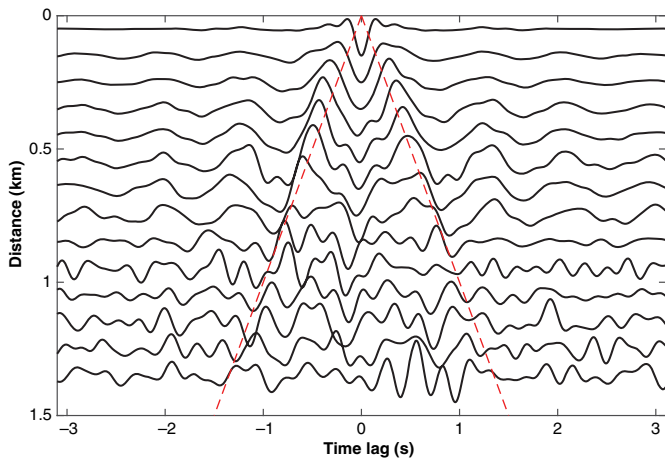


Figure 7. Bin stacked CCF record section. All available CCFs on 5 July are used. The dashed lines depict the 1 km/s reference velocity used in the back projection analysis. The color version of this figure is available only in the electronic edition.

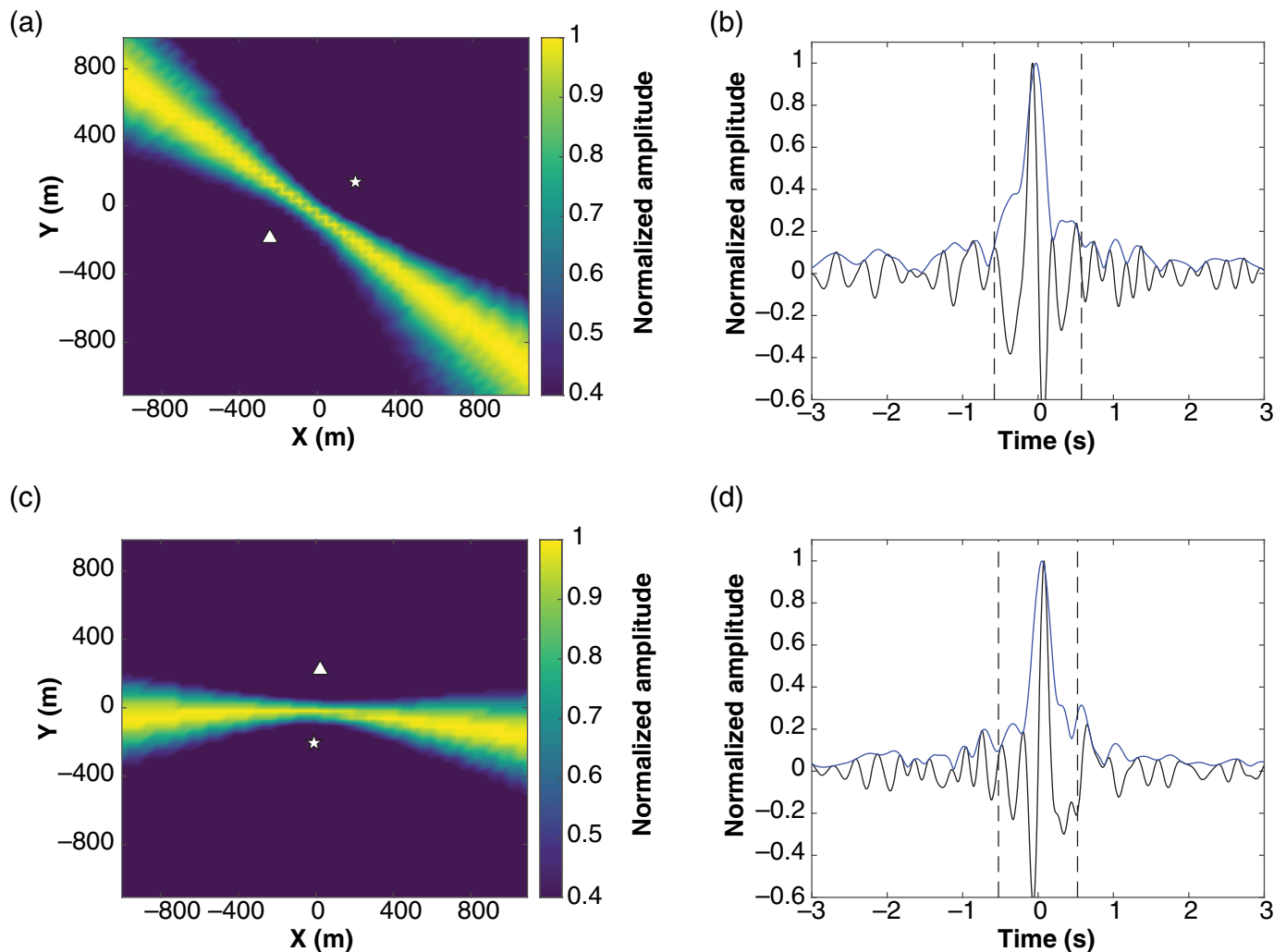


Figure 8. (a) The likelihood source location map derived from the 2D back projection of an example 5-min CCF of station pair 8–5. The star and the triangle depict the virtual source (station 8) and the receiver (station 5), respectively. (b) The 5-min CCF waveform (black line) and envelope (blue solid line) used in

We take the same 5-min time window as in Figure 9b (00:15–00:20 of 7/26) to demonstrate the 3D back projection result (Fig. 12). Like the 2D case, a good agreement is observed between the likelihood area and the cataloged event locations. The majority of the cataloged seismicity is contained by the 0.9 normalized amplitude area. Comparing the locations at 0, 200, and 400 m depth (Figs. 10b and 12a,b), the 3D back-projection shows an advantage in ruling out the deeper sources (>500 m); however, sources at shallow depth cannot be distinguished as the high likelihood area in general is elongated vertically and dips slightly toward the northwestern direction. The overall lower vertical resolution near the surface compared to the lateral resolution is expected for shallow sources considering the shape of 3D hyperboloids with both foci at the surface (Fig. 11).

The 3D result provides some constraints to the source depth, despite the maximum likelihood area being slightly shallower than the cataloged event depths. The maximum amplitude in

panel (a). The dashed lines denote the signal time window used in the back projection, which is determined based on the source–receiver distance and the 1 km/s reference velocity. (c,d) Same as panels (a,b) but for station pair 6–3. The color version of this figure is available only in the electronic edition.

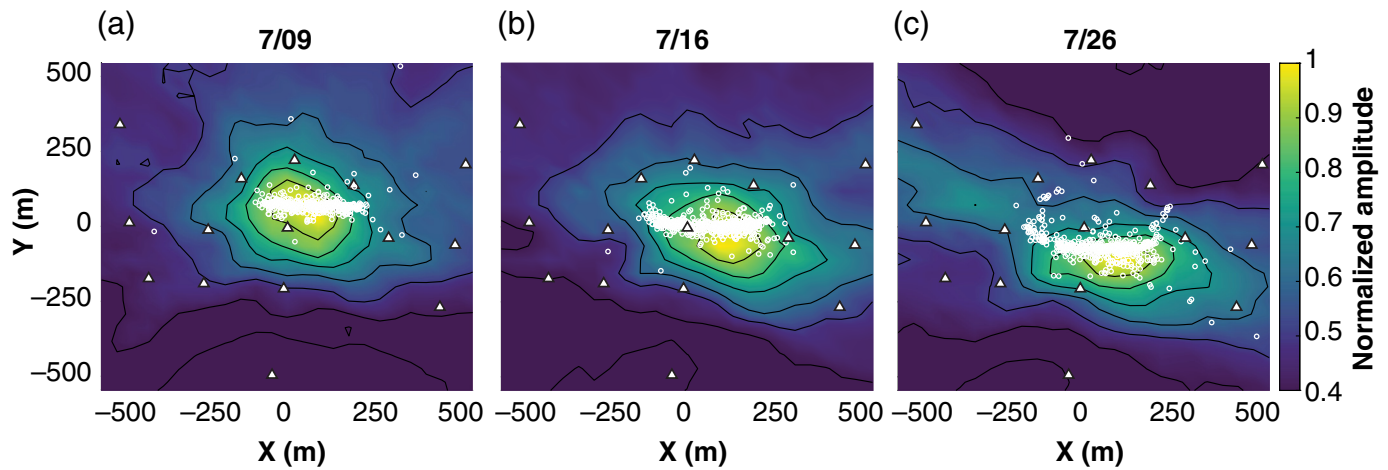


Figure 9. The likelihood source location maps on (a) 7/09, (b) 7/16, and (c) 7/26 derived from 2D back projection using all daily CCFs. The white open circles depict the corresponding daily seismicity, white triangles

represent the stations, and the contours are plotted with an increment of 0.1 normalized amplitude. The rest of the days are shown in Movie S1. The color version of this figure is available only in the electronic edition.

Figure 12b,d is around 150–200 m, whereas the cataloged seismic activity is between 200 and 250 m depth. In addition to intrinsic low vertical resolution, the use of a homogeneous

reference velocity and the likely entanglement of different wave types can also contribute to the apparent discrepancy. We note that our result nevertheless rules out deep sources consistent

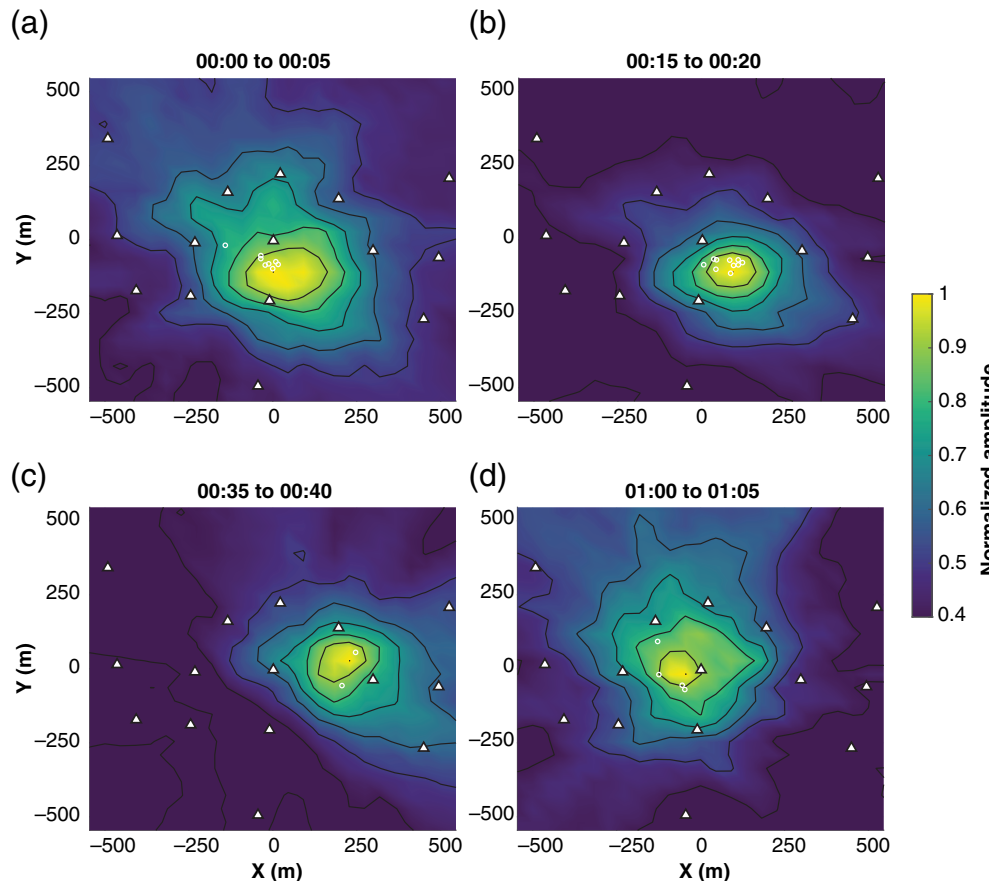


Figure 10. Same as Figure 9 but for 5-min CCFs on 26 July. (a) From 00:00 to 00:05. (b) From 00:15 to 00:20. (c) From 00:35 to 00:40. (d) From 01:00 to 01:05. The color version of this figure is available only in the electronic edition.

with mostly shallow mining related activities. The depth resolution (e.g., the plausible area with normalized amplitude >0.9) of the 3D result is larger than the 2D lateral resolution by a factor of 3, and the 3D computation time increases dramatically compared to 2D due to the 3D grid search. Consequently we feel the 2D framework might be more robust and better suited for automated seismic monitoring in a variety of environments (e.g., volcanic, geothermal, hydrothermal, mining, and wastewater or CO₂ injection) although 3D analysis can be used to provide additional depth constraints.

CONCLUSIONS

We collected one month of passive seismic data from a surface array above an active longwall coal mine. The continuous seismic recording dominantly consists of long-period (5–10 s) energy from microseism and short-period

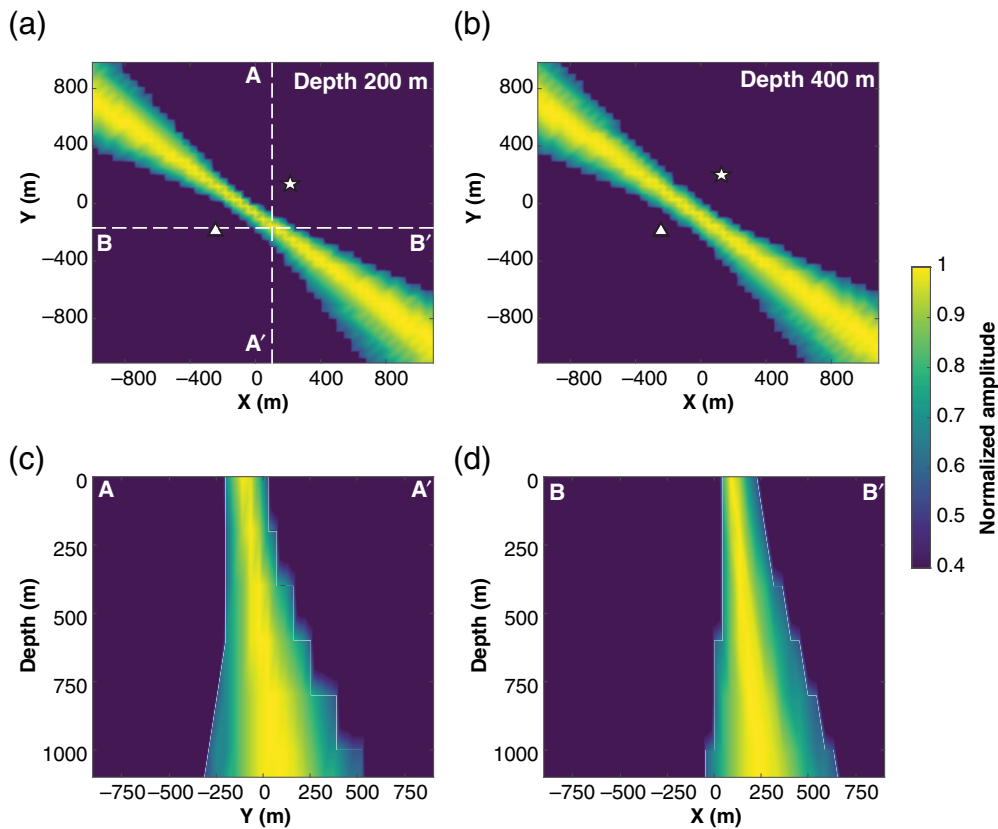


Figure 11. Similar to Figure 8a but for 3D back projection. (a,b) The likelihood normalized amplitude maps at 200 and 400 m depths. (c,d) The north–south cross section (A–A’ profile in panel a) and the east–west cross section (B–B’ profile in panel a), respectively. The color version of this figure is available only in the electronic edition.

(>1 Hz) energies from induced seismicity, industrial equipment, and background noise. We present a method to separate the mining-related activity from background noise by seismic interferometry and waveform similarity. Specifically, we classify the correlation coefficients between the monthly stacked CCFs and the consecutive 5-min window CCFs into two groups. The low correlation coefficient CCFs correspond to time windows dominated by background noise and are mostly stationary over time. In contrast, the high correlation coefficient CCFs correspond to time windows with mine activity and exhibit a temporal variation in line with the progression of the mining operation.

We migrate and back project the 5-min and daily cross-correlation wave packets from the high correlation coefficient time windows to locate the underground mining activity throughout the one-month deployment period. The resolved locations from both time resolutions correlate well with the cataloged seismic activity of the mine and the evolution of the longwall location. We show that our analysis has the ability to distinguish source clusters that are 200 m and 5 min apart. The consistency between the resolved noise location, seismicity, and longwall progression indicates the ability of the method to track small

changes in source migration. The interferometry and back projection approach presented in this study can be a low-cost, computationally inexpensive, and reliable framework to monitor and distinguish seismic sources in an active environment (e.g., mine, volcano, geothermal or hydrothermal system, fracking or wastewater injection site, and oil or gas extraction area). Further work is needed to characterize and locate seismic activity of higher frequency where scattering and multipathing effects need to be accounted for. The background noise CCFs isolated from time windows with mining activity can be used to study temporal structural variation that might be sensitive to the mine caving process.

DATA AND RESOURCES

Raw data were collected at the mine site under conditions of anonymity and therefore cannot be released to the public. Cross-correlation functions (CCFs) are available upon

request and decontextualized event waveforms are available at <https://doi.org/10.7910/DVN/5DGFJB>. Most of the plots were made using MATLAB v. 9.7.0.1190202 (R2019b). The supplemental material contains a video showing the likelihood source location maps from 2D back projection using daily stacks of CCFs (complement to Fig. 8). The white open circles depict the corresponding daily seismicity, the white triangles represent the stations, and the contours are plotted with an increment of 0.1 normalized amplitude.

DECLARATION OF COMPETING INTERESTS

The authors acknowledge that there are no conflicts of interest recorded.

ACKNOWLEDGMENTS

The authors thank the Associate Editor and two anonymous reviewers for their constructive comments to improve the article. The authors gratefully acknowledge the National Institute for Occupational Safety and Health (NIOSH) and an anonymous collaborating mine site for permitting us to use this dataset. This study was supported by the National Science Foundation (NSF) Grant EAR 1753362 and NIOSH project 19IPA1916693. S. R. acknowledges a scholarship by the *Consejo Nacional de Ciencia y Tecnología* (CONACYT; Scholarship Number 710069). The findings and conclusions in this

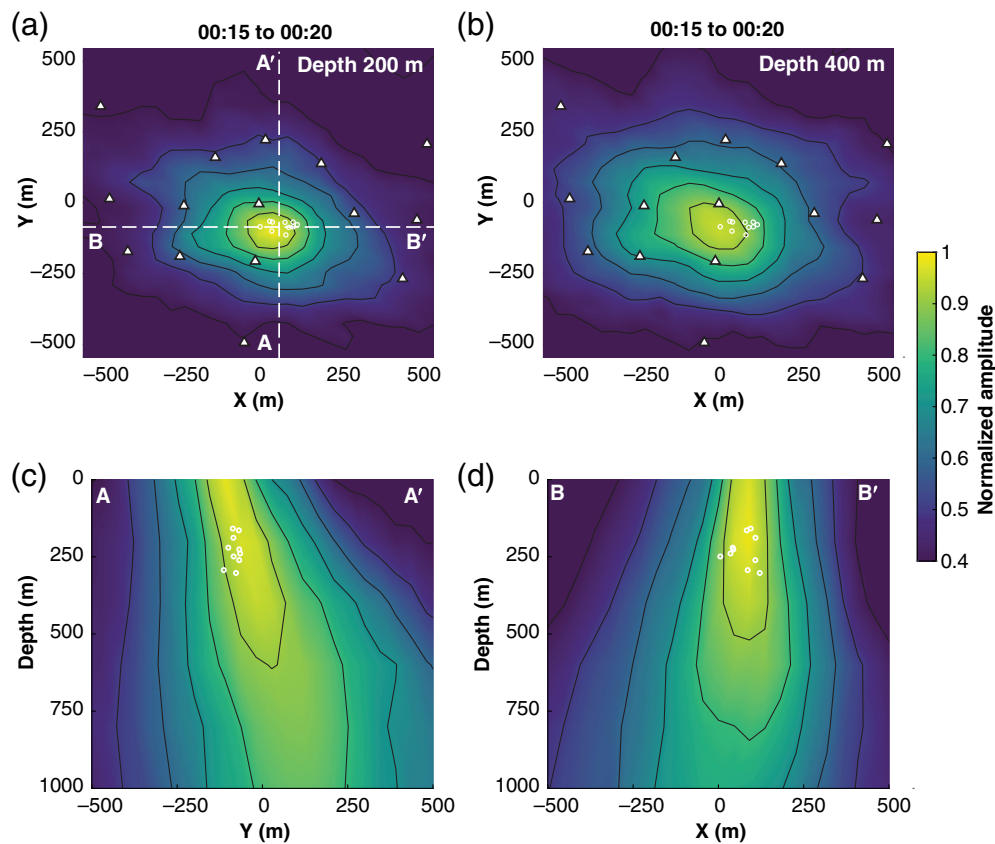


Figure 12. Similar to Figure 10b but for 3D back projection. (a,b) The likelihood normalized amplitude maps at 200 and 400 m depths. (c,d) The north–south cross section (A–A' profile in panel a) and the east–west cross section (B–B' profile in panel a), respectively. The color version of this figure is available only in the electronic edition.

report are those of the author(s) and do not necessarily represent the official position of the National Institute for Occupational Safety and Health, Centers for Disease Control and Prevention. Mention of any company or product does not constitute endorsement by NIOSH, CDC.

REFERENCES

- Ballmer, S., C. J. Wolfe, P. G. Okubo, M. M. Haney, and C. H. Thurber (2013). Ambient seismic noise interferometry in Hawai'i reveals long-range observability of volcanic tremor, *Geophys. J. Int.* **194**, no. 1, 512–523, doi: [10.1093/gji/ggt112](https://doi.org/10.1093/gji/ggt112).
- Bischoff, M., A. Cete, R. Fritschen, and T. Meier (2010). Coal mining induced seismicity in the Ruhr area, Germany, *Pure Appl. Geophys.* **167**, nos. 1/2, 63–75, doi: [10.1007/s00024-009-0001-8](https://doi.org/10.1007/s00024-009-0001-8).
- Brenguier, F., M. Campillo, C. Hadziioannou, N. M. Shapiro, R. M. Nadeau, and E. Larose (2008). Postseismic relaxation along the San Andreas fault at Parkfield from continuous seismological observations, *Science* **321**, no. 5895, 1478–1481, doi: [10.1126/science.1160943](https://doi.org/10.1126/science.1160943).
- Bowden, D.C., V.C. Tsai, and F.-C. Lin, (2015). Site amplification, attenuation and scattering from noise correlation amplitudes across a dense array in Long Beach, *Geophys. Res. Lett.* **42**, 1360–1367, doi: [10.1002/2014GL062662](https://doi.org/10.1002/2014GL062662).

- Chen, B. R., X. T. Feng, X. Zeng, Y. Xiao, Z. Zhang, H. Ming, and G. Feng (2011). Real-time microseismic monitoring and its characteristic analysis during TBM tunneling in deep-buried tunnel, *Chin. J. Rock Mech. Eng.* **30**, no. 2, 275–283.
- Clements, T., and M. A. Denolle (2018). Tracking groundwater levels using the ambient seismic field, *Geophys. Res. Lett.* **45**, no. 13, 6459–6465, doi: [10.1029/2018GL077706](https://doi.org/10.1029/2018GL077706).
- Cros, E., P. Roux, J. Vandemeulebrouck, and S. Kedar (2011). Locating hydrothermal acoustic sources at old faithful geyser using matched field processing, *Geophys. J. Int.* **187**, no. 1, 385–393, doi: [10.1111/j.1365-246X.2011.05147.x](https://doi.org/10.1111/j.1365-246X.2011.05147.x).
- Czarny, R., H. Marcak, N. Nakata, Z. Pilecki, and Z. Isakow (2016). Monitoring velocity changes caused by underground coal mining using seismic noise, *Pure and Appl. Geophys.* **173**, no. 6, 1907–1916.
- Dales, P., P. Audet, and G. Olivier (2017a). Seismic interferometry using persistent noise sources for temporal subsurface monitoring, *Geophys. Res. Lett.* **44**, no. 21, 10,863–10,870, doi: [10.1002/2017GL075342](https://doi.org/10.1002/2017GL075342).
- Dales, P., P. Audet, G. Olivier, and J. P. Mercier (2017b). Interferometric methods for spatio temporal seismic monitoring in underground mines, *Geophys. J. Int.* **210**, no. 2, 731–742, doi: [10.1093/gji/ggx189](https://doi.org/10.1093/gji/ggx189).
- Eaton, D. W. (2018). *Passive Seismic Monitoring of Induced Seismicity: Fundamental Principles and Application to Energy Technologies*, Cambridge University Press, Cambridge, United Kingdom.
- Haney, M. M. (2010). Location and mechanism of very long period tremor during the 2008 eruption of Okmok volcano from interstation arrival times, *J. Geophys. Res.* **115**, no. 10, 1–13, doi: [10.1029/2010JB007440](https://doi.org/10.1029/2010JB007440).
- Haney, M. M. (2014). Backprojection of volcanic tremor, *Geophys. Res. Lett.* **41**, no. 6, 1923–1928, doi: [10.1002/2013GL058836](https://doi.org/10.1002/2013GL058836).
- Johnson, S. W., D. J. Chambers, M. S. Boltz, and K. D. Koper (2021). Application of a convolutional neural network for seismic phase picking of mining-induced seismicity, *Geophys. J. Int.* **224**, no. 1, 230–240.
- Kao, H., and S. J. Shan (2004). The source-scanning algorithm: Mapping the distribution of seismic sources in time and space, *Geophys. J. Int.* **157**, no. 2, 589–594, doi: [10.1111/j.1365-246X.2004.02276.x](https://doi.org/10.1111/j.1365-246X.2004.02276.x).
- Li, K. L., H. Sadeghisorkhani, G. Sgattioni, O. Gudmundsson, and R. Roberts (2017). Locating tremor using stacked products of

- correlations, *Geophys. Res. Lett.* **44**, no. 7, 3156–3164, doi: [10.1002/2016GL072272](https://doi.org/10.1002/2016GL072272).
- Li, L., J. Tan, B. Schwarz, F. Staněk, N. Poiata, P. Shi, L. Diekmann, L. Eisner, and D. Gajewski (2020). Recent advances and challenges of waveform-based seismic location methods at multiple scales, *Rev. Geophys.* **58**, no. 1, 1–47, doi: [10.1029/2019RG000667](https://doi.org/10.1029/2019RG000667).
- Lin, F. C., M. P. Moschetti, and M. H. Ritzwoller (2008). Surface wave tomography of the western United States from ambient seismic noise: Rayleigh and Love wave phase velocity maps, *Geophys. J. Int.* **173**, no. 1, 281–298, doi: [10.1111/j.1365-246X.2008.03720.x](https://doi.org/10.1111/j.1365-246X.2008.03720.x).
- Lin, F.-C., V. Tsai, and M.H. Ritzwoller (2012). The local amplification of surface waves: A new observable to constrain elastic velocities, density, and anelastic attenuation, *J. Geophys. Res.* **117**, no. B6, doi: [10.1029/2012JB009208](https://doi.org/10.1029/2012JB009208).
- Lobkis, O. I., and R. L. Weaver (2001). On the emergence of the Green's function in the correlations of a diffuse field, *J. Acoust. Soc. Am.* **110**, no. 6, 3011–3017, doi: [10.1121/1.1417528](https://doi.org/10.1121/1.1417528).
- Lu, B., and J. Feng (2017). Coal working face imaging by seismic interferometry-using conveyor belt noise as source, *J. Seismol. Explor.* **26**, no. 5, 411–432.
- Majer, E. L., R. Baria, M. Stark, S. Oates, J. Bommer, B. Smith, and H. Asanuma (2007). Induced seismicity associated with enhanced geothermal systems, *Geothermics* **36**, no. 3, 185–222, doi: [10.1016/j.geothermics.2007.03.003](https://doi.org/10.1016/j.geothermics.2007.03.003).
- Maxwell, S. C., D. Raymer, M. Williams, and P. Primiero (2012). Tracking microseismic signals from the reservoir to surface, *The Leading Edge* **31**, no. 11, 1300–1308, doi: [10.1190/tle31111300.1](https://doi.org/10.1190/tle31111300.1).
- Mendecki, A. J., R. A. Lynch, and D. A. Malovichko (2010). Routine micro-seismic monitoring in mines, *Australian Earthquake Engineering Society 2010 Conference*, November 2010, Perth, Australia, 1–33.
- Nicolson, H., A. Curtis, and B. Baptie (2014). Rayleigh wave tomography of the British Isles from ambient seismic noise, *Geophys. J. Int.* **198**, no. 2, 637–655, doi: [10.1093/gji/ggu071](https://doi.org/10.1093/gji/ggu071).
- Nordström, E., S. Dineva, and E. Nordlund (2020). Back analysis of short-term seismic hazard indicators of larger seismic events in deep underground mines (LKAB, Kiirunavaara mine, Sweden), *Pure Appl. Geophys.* **177**, no. 2, 763–785.
- Sen, A. T., S. Cesca, M. Bischoff, T. Meier, and T. Dahm (2013). Automated full moment tensor inversion of coal mining-induced seismicity, *Geophys. J. Int.* **195**, no. 2, 1267–1281, doi: [10.1093/gji/ggt300](https://doi.org/10.1093/gji/ggt300).
- Shapiro, N. M., M. Campillo, L. Stehly, and M. H. Ritzwoller (2005). High-resolution surface-wave tomography from ambient seismic noise, *Science* **307**, no. 5715, 1615–1618, doi: [10.1126/science.1108339](https://doi.org/10.1126/science.1108339).
- Shapiro, N. M., M. H. Ritzwoller, and G. D. Bensen (2006). Source location of the 26 sec microseism from cross-correlations of ambient seismic noise, *Geophys. Res. Lett.* **33**, no. 18, 1–5, doi: [10.1029/2006GL027010](https://doi.org/10.1029/2006GL027010).
- Spica, Z., M. Pertou, M. Calò, D. Legrand, F. Córdoba-Montiel, and A. Iglesias (2016). 3-D shear wave velocity model of Mexico and south US: Bridging seismic networks with ambient noise cross-correlations (C1) and correlation of coda of correlations (C3), *Geophys. J. Int.* **206**, no. 3, 1795–1813, doi: [10.1093/gji/ggw240](https://doi.org/10.1093/gji/ggw240).
- Stec, K. (2007). Characteristics of seismic activity of the upper Silesian coal basin in Poland, *Geophys. J. Int.* **168**, no. 2, 757–768, doi: [10.1111/j.1365-246X.2006.03227.x](https://doi.org/10.1111/j.1365-246X.2006.03227.x).
- Stehly, L., M. Campillo, and N. M. Shapiro (2006). A study of the seismic noise from its long-range correlation properties, *J. Geophys. Res.* **111**, no. 10, 1–12, doi: [10.1029/2005JB004237](https://doi.org/10.1029/2005JB004237).
- Swanson, P. L., M. S. Boltz, and D. Chambers (2016). Seismic monitoring strategies for deep longwall coal mines, Department of Health and Human Services Centers for Disease Control and Prevention National Institute for Occupational Safety and Health, Office of Mine Safety and Health Research Pittsburgh, Spokane, Washington.
- Verdon, J. P., J. M. Kendall, A. Butcher, R. Lockett, and B. J. Baptie (2018). Seismicity induced by longwall coal mining at the Thoresby Colliery, Nottinghamshire, U.K., *Geophys. J. Int.* **212**, no. 2, 942–954, doi: [10.1093/gji/ggx465](https://doi.org/10.1093/gji/ggx465).
- Verdon, J. P., J. M. Kendall, and S. C. Maxwell (2010). A comparison of passive seismic monitoring of fracture stimulation from water and CO₂ injection, *Geophysics* **75**, no. 3, 1–7, doi: [10.1190/1.3377789](https://doi.org/10.1190/1.3377789).
- Wu, S. M., F. C. Lin, J. Farrell, and A. Allam (2019). Imaging the deep subsurface plumbing of old faithful geyser from low-frequency hydrothermal tremor migration, *Geophys. Res. Lett.* **46**, no. 13, 7315–7322, doi: [10.1029/2018GL081771](https://doi.org/10.1029/2018GL081771).
- Wu, S. M., F. C. Lin, J. Farrell, W. E. Keller, E. B. White, and J. D. G. Hungerford (2021). Imaging the subsurface plumbing complex of steamboat geyser and cistern spring with hydrothermal tremor migration using seismic interferometry, *J. Geophys. Res.* **126**, no. 4, doi: [10.1029/2020JB021128](https://doi.org/10.1029/2020JB021128).
- Wu, S. M., F. C. Lin, J. Farrell, B. Shiro, L. Karlstrom, P. Okubo, and K. Koper (2020). Spatiotemporal seismic structure variations associated with the 2018 Kilauea eruption based on temporary dense geophone arrays, *Geophys. Res. Lett.* **47**, no. 9, 1–10, doi: [10.1029/2019GL086668](https://doi.org/10.1029/2019GL086668).
- Wu, S. M., K. M. Ward, J. Farrell, F. C. Lin, M. Karplus, and R. B. Smith (2017). Anatomy of old faithful from subsurface seismic imaging of the Yellowstone upper Geyser basin, *Geophys. Res. Lett.* **44**, no. 20, 240–247, doi: [10.1002/2017GL075255](https://doi.org/10.1002/2017GL075255).
- Zheng, Y., W. Shen, L. Zhou, Y. Yang, Z. Xie, and M. H. Ritzwoller (2011). Crust and uppermost mantle beneath the north China craton, northeastern China, and the Sea of Japan from ambient noise tomography, *J. Geophys. Res.* **116**, no. 12, 1–25, doi: [10.1029/2011JB008637](https://doi.org/10.1029/2011JB008637).

Manuscript received 3 March 2022

Published online 28 June 2022